Large magnetic anisotropy in ferrihydrite nanoparticles synthesized from reverse micelles

INSTITUTE OF PHYSICS PUBLISHING NANOTECHNOLOGY
Nanotechnology **17** (2006) 5549–5555 doi:10.1088/0957-4484/17/22/004

Large magnetic anisotropy in ferrihydrite nanoparticles synthesized from reverse micelles

E L Duarte[1], R Itri[1], E Lima Jr[1], M S Baptista[2], T S Berquó[3] and G F Goya[4,5]

[1] Instituto de Física, Universidade de São Paulo, CP 66318, São Paulo, 05315-970, Brazil
[2] Instituto de Química, Universidade de São Paulo, Avenida Professor Lineu Prestes 748, São Paulo, Brazil
[3] Institute for Rock Magnetism, University of Minnesota, 100 Union Street SE, Minneapolis, MN 55455-0128, USA
[4] Instituto de Nanociencias de Aragón (INA), Universidad de Zaragoza, Pedro Cerbuna 12, (50009), Zaragoza, Spain

E-mail: goya@unizar.es

Received 13 June 2006, in final form 24 September 2006
Published 25 October 2006
Online at stacks.iop.org/Nano/17/5549

Abstract
Six-line ferrihydrite (FH) nanoparticles have been synthesized in the core of reverse micelles, used as nanoreactors to obtain average particle sizes $\langle d \rangle \approx 2$–4 nm. The blocking temperatures T_B^m extracted from magnetization data increased from ≈10 to 20 K for increasing particle size. Low-temperature Mössbauer measurements allowed us to observe the onset of differentiated contributions from the particle core and surface as the particle size increases. The magnetic properties measured in the liquid state of the original emulsion showed that the ferrihydrite phase is not present in the liquid precursor, but precipitates in the micelle cores after the free water is freeze-dried. Systematic susceptibility $\chi_{ac}(f, T)$ measurements showed the dependence of the effective magnetic anisotropy energies E_a with particle volume, and yielded an effective anisotropy value of $K_{eff} = 312 \pm 10$ kJ m^{-3}.

1. Introduction

Ferrihydrite is a poorly crystalline Fe^{3+} oxyhydroxide whose detailed crystal structure has remained elusive up to now, as reflected by the identification of the known phases as 'two-line' and 'six-line' on the basis of their two or six broad x-ray diffraction (XRD) peaks. It has been proposed that the two-line type consists of extremely small crystalline domains, whereas the six-line type has larger crystal domains of hexagonal structure with unit-cell parameters $a = 2.96$ Å, $c = 9.40$ Å [1]. More recently, Jansen *et al* [2] have refined their XRD data by considering a space group $P1c$ phase plus a defective phase with space group $P3$. Electron microscopy and Mössbauer spectroscopy have been employed quite successfully for identifying the properties of both kind of structures regarding their local structural and magnetic properties [3–6]. These works on ferrihydrite have consistently provided a landscape in which some aggregates with ordered structure, with small regions of ≈2–3 nm, display definite lattice fringes and a narrow distribution of hyperfine parameters. This iron oxyhydroxide phase is found in many biological systems (e.g., iron-reducing bacteria, *Aedes aegypti* mosquito), as well as in hydrometallurgical operations (as an undesired precipitate) [7]. Along with the interest of the basic physical mechanisms governing the structure and surface formation, ferrihydrite also has significance because it constitutes the core of ferritin, a protein that plants and animals use to sequester and store iron, providing a fully biocompatible material to carry iron particles in potential drug delivery applications [8].

Regarding the magnetic properties of ferrihydrite, many reported studies on its behaviour are based on its biological complex ferritin, using either ^{57}Fe Mössbauer

[5] On leave from: Physics Institute, University of Sao Paulo, Brazil.

spectroscopy [9, 10] or magnetization measurements [11, 12]. The main results point to a cluster-like structure with Fe^{3+} ions antiferromagnetically ordered within the core and a small uncompensated magnetic moment (probably at the particle surface). But the actual physical units from which the observed cluster or superparamagnetic (SPM) behaviour is originated have not been univocally defined.

For antiferromagnetic (AFM) particles of diameter a few nanometres, a small uncompensated magnetic moment is expected to arise from defects within the particle and/or from the unpaired surface moments of the particle [13]. The net magnetic moment of the particle reverses between different spatial orientations with a characteristic time τ that depends on the temperature and particle volume. Within Néel's model [14] the probability of switching the particle's magnetic moment is a thermally activated process described by

$$\tau = \tau_0 \exp\left(-\frac{E_a}{k_B T}\right), \qquad (1)$$

where E_a is the energy barrier that separates two energy minima between magnetization states (up and down), and k_B is the Boltzmann constant. The pre-exponential parameter τ_0 is usually assumed to be of the order of 10^{-9}–10^{-11} s, and dependent on the reversal mechanism [15, 16].

In this work we present a characterization of ferrihydrite particles with different average diameters ranging from about 2 to 4 nm, synthesized using reverse micelles as nanoreactors with the aim to have a particle volume control. Reverse micelles (RMs) consist of nanometre-sized aqueous droplets suspended in a nonpolar continuous organic phase by surfactant shells. The size of the water cores is determined by the water-to-surfactant molar ratio, W. Some aqueous phase reactions, including chemical precipitation of solid particles, can be accomplished in the micelle core. In particular, the RM has been successfully employed as a nanoreactor in the synthesis of some ferrites (magnetite, $CoFe_2O_4$, $ZnFe_2O_4$, $MnFe_2O_4$ among others) by several groups [17–19]. However, after the precursor is formed in the micellar core, it is extracted and submitted to a thermal treatment to reach the desired compound with diameters ranging from 10 to 20 nm. In our case, we have realized that such precursor is, indeed, made up of six-line ferrihydrite nanoparticles with size diameters smaller than 4 nm depending on W. To the best of our knowledge, this is the first time that the magnetic properties of this kind of ferrihydrite synthesized in the core of RMs is reported. The main objective is to investigate the contribution of the finite size and surface effects on the magnetic properties through their evolution for increasing particle size.

2. Materials and methods

2.1. Chemicals and synthesis

Surfactant sodium bis(*2-ethylhexyl*) sulfosuccinate (AOT) was purchased from Fluka Chemicals; isooctane was from Synth, tetra hydrated ferrous chloride ($FeCl_2{\cdot}4H_2O$) and sodium hydroxide (NaOH) were from Merck. All reagents were used as received. Water was distilled in an all-glass apparatus, filtered and deionized (Milli-Q water). Ethanol and acetone were used during the extraction process of nanoparticles from

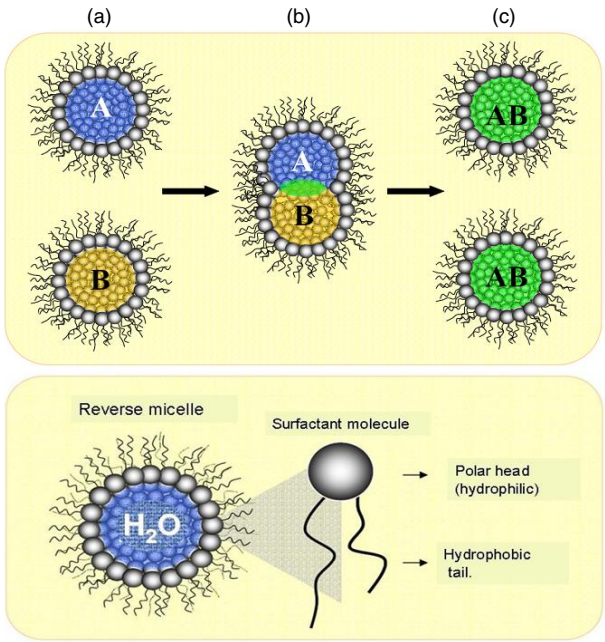

Figure 1. Schematic diagram showing the reverse micelle synthesis of ferrihydrite: the two reverse micelle solutions (a) with A and B contents of their aqueous phases are mixed (b) and stirred, to exchange aqueous material and form AB solution. The surfactant-to-water ratio W controls the micelle diameter, and therefore the final particle sizes (c).

(This figure is in colour only in the electronic version)

RMs. All experiments were performed at room temperature of 23(1) °C.

The protocol for synthesizing nanoparticles in a micellar environment is well known in the literature [20, 21], and consists in mixing two RM solutions with the same surfactant composition, but differing in the content of their aqueous phases, as shown schematically in figure 1. In our case, both micellar solutions were composed of 0.4 M AOT in isooctane, one of them containing 0.05 M aqueous solution of $FeCl_2$ and the other 0.20 M of sodium hydroxide aqueous solution. For the mixture, 200 ml of the RM solution containing $FeCl_2$ was vigorously stirred, whereas 200 ml of the RM solution containing NaOH was added dropwise. The final solution was further stirred for two hours to complete the homogenization. The solution's colour changes from bright yellow to dark brown, indicating the formation of iron oxide particles [18, 19]. Four different samples were synthesized, labelled by the molar ratio between AOT and the aqueous concentration as W = [water]/[AOT], with W values of 10, 15, 20 and 30 (see table 1). In order to extract the synthesized iron oxide nanoparticles from the RM, the *isooctane* was firstly evaporated by means of a rotoevaporator. Then, the sample was washed several times with ethanol to remove the surfactant by centrifuging. Finally, the samples were washed with acetone to improve the drying. All samples were stored at room temperature and low pressure in a camera containing silica gel. Elemental analysis indicated that the resulting dried powders contained about 12 wt% of C in their composition. The presence of C atoms in the synthesized sample is due to the surfactant residues not being well eliminated in the washing

Table 1. Magnetic and hyperfine parameters for samples with average grain sizes $\langle d \rangle_{XRD}$ as estimated from XRD data: blocking temperature T_B^m; coercive field H_C, energy barrier E_a^{zfc}, and energy barrier E_a^{ac}. Hyperfine parameters from the distribution fit of figure 5: isomer shift (IS); hyperfine field at the distribution maximum (B_{max}); average hyperfine field (B_{mean}) and variance $\mathfrak{V}$ of the fitted distribution.

Sample	$W = \frac{[H_2O]}{[AOT]}$	$\langle D \rangle_{XRD}$ (nm)	T_B^m (K)[a]	E_a^{ZFC} ($\times 10^{-21}$ J)[a]	H_C (5 K) (kOe)	E_a^{ac} ($\times 10^{-21}$ J)[b]	IS (mm s^{-1})	B_{max} (T)	B_{mean} (T)	$\mathfrak{V}$ (au)
W10	10	2.4(1)	10.4(5)	4.5(3)	1.23(9)	3.1(3)	0.42(1)	47.1(1)	44.5	3470
W15	15	3.2(1)	17.4(5)	7.8(4)	1.22(9)	5.0(4)	0.42(1)	48.3(1)	46.6	2336
W20	20	3.1(1)	20.1(5)	10.1(3)	1.22(9)	6.6(3)	0.43(1)	48.5(1)	46.8	2004
W30	30	3.9(1)	29.5(5)	16.5(5)	1.13(9)	11.7(7)	0.41(1)	48.7(1)	46.9	1706

[a] From ZFC curves, see text and figure 6.
[b] From $\chi(f, T)$ data.

process; they might remain attached to the nanoparticle surface.

2.2. Apparatus

X-ray diffraction (XRD) was used to investigate the crystallographic structure of the powder samples. The experiments were performed by means of a Rigaku-Denki powder diffractometer with a conventional x-ray generator (Cu Kα radiation, $\lambda = 1.5418$ Å and a graphite monochromator) coupled to a scintillation detector. The angular scanning performed on all samples ranged from 20° up to 70° with 0.05° step-widths. The average particle diameter (d_{XRD}) was calculated from the full width at half maximum of the more intense reflection using Scherrer's equation [22].

Mössbauer spectroscopy (MS) measurements were performed between 4.2 and 296 K in a liquid He flow cryostat, with a conventional constant-acceleration spectrometer in transmission geometry. The spectra were fitted to Lorentzian line shapes using a nonlinear least-squares program, calibrating the velocity scale with a foil of α-Fe at 296 K. When necessary, distributions of the hyperfine magnetic fields, isomer shift and quadrupole splitting were used to fit the spectra. Magnetization and ac magnetic susceptibility measurements were performed in a commercial SQUID magnetometer both in zero-field-cooling (ZFC) and field-cooling (FC) modes (always in the heating direction) between 1.8 K $< T <$ 250 K and under applied fields up to 9 T. The frequency dependence of both in-phase $\chi'(T)$ and out-of-phase $\chi''(T)$ components of the ac magnetic susceptibility was measured by using an excitation field of 1–4 G and driving frequencies 0.01 Hz $\leqslant f \leqslant$ 1500 Hz.

3. Experimental results

3.1. Structural analysis and particle dimension

X-ray profiles performed on dried powders showed two prominent peaks at $2\theta \sim 35.5°$ and ~61.5°, as indicated by the arrows in the figure 2, corresponding to q values of 2.49 Å^{-1} and 4.17 Å^{-1}, respectively. The broad peak at ~61.5° seems to be two peaks combined. Additionally, small peaks at ~41.1° and ~53.7° can be noticed, and also a very small feature at ~47°. These features on the XRD pattern agree with a six-line ferrihydrite phase [23]. The sample W10 presents additional peaks that are identified as diffraction peaks from Na_2SO_4 crystals. This phase is likely to be formed during the AOT extraction process, since it is known that at the

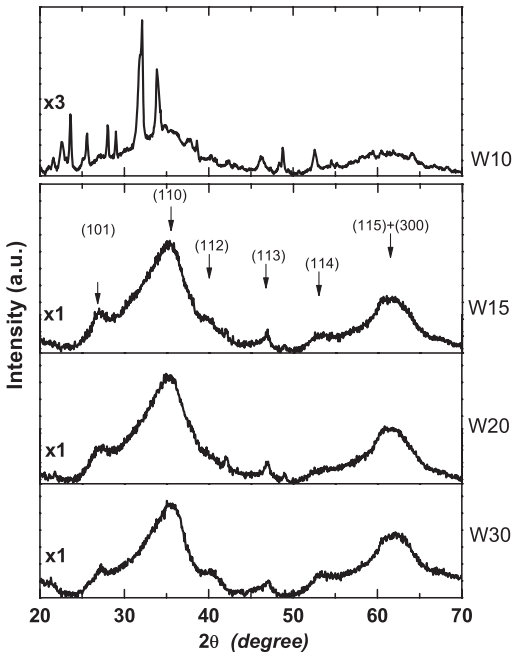

Figure 2. X-ray powder diffraction data from the four samples synthesized using reverse micelles at $W = 10$, 15, 20 and 30. The peak positions of the two-line (full arrows) plus the additional ones for the six-line (open arrows) ferrihydrite structure are shown at the top of the figure.

values for sample W10 all water in the pool is strongly bound and there is a high local amount of hydroxyl ions (related to the AOT hydrolysis process). When a nanoparticle grows in this environment, it must also be strongly bound to the hydrolysed AOT polar head, yielding Na_2SO_4 formation on the nanoparticle surface. This is not observed at the concentration ratios for samples W15 to W30 because the presence of bulk water facilitates the nanoparticle solvation and a decrease in concentration of local hydroxyl ions.

Because of the low crystallinity of ferrihydrites, the broad peaks cannot be directly used for an accurate determination of the particle size through the Scherrer formula, so further transmission electron microscopy (TEM) images were used to better define the particle dimensions. Figure 3 shows as an example a TEM micrograph from sample W15. All images were recorded with a slow scan CCD camera (Proscan) and processed in the AnalySis 3.0 software that allows one to work with enhanced images in such a way that particle-by-particle size measurement can be performed with high precision.

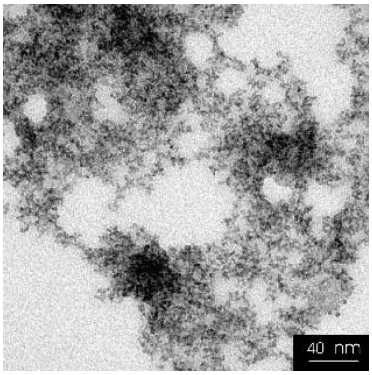

Figure 3. TEM micrograph recorded from sample W15.

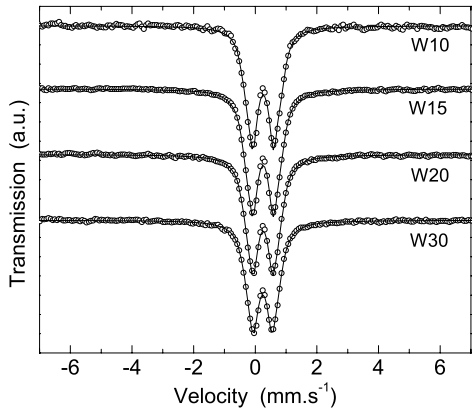

Figure 4. Mössbauer spectra taken at room temperature for samples W10 to W30. Open symbols are the experimental points, and solid lines the fitted spectra.

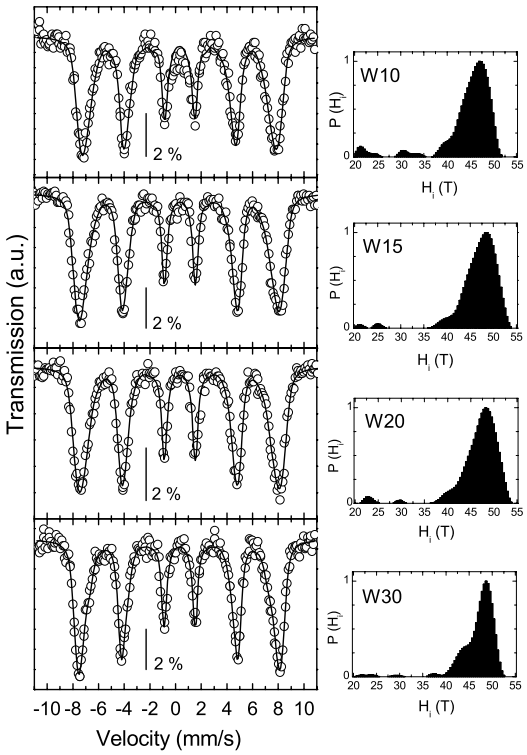

Figure 5. Fitted Mössbauer spectra at $T = 4.2$ K for samples W10 to W30 using a distribution of fields. Open symbols are the experimental data, and solid lines the fitted spectra. The bars indicate the amount of resonant effect (per cent) for each spectrum. The right column shows the resulting histogram for the obtained hyperfine field B_{hyp}.

Table 1 contains the average particle diameter d_{XRD} obtained from the diffraction data, calculated from the broad diffraction peak at $2\theta \sim 35.5°$. The resulting values were compatible with the mean values observed in electron microscope images and expected for six-line ferrihydrites [7, 23]. Note that the average size seems to increase from sample W10 to sample W30, suggesting that the micelle pool features might, in our case, define the iron oxide based nanoparticle size.

3.2. Mössbauer measurements

In the SPM state the magnetic hyperfine interactions are averaged to zero due to fast relaxation of the particle magnetic moments, so the resulting Mössbauer spectra consist of a paramagnetic-like doublet. Accordingly, the room temperature spectra recorded for samples W10 to W30 (figure 4) showed the expected doublet, with essentially identical hyperfine parameters, i.e., quadrupole splitting QS = 0.60–0.63(2) mm s^{-1} and isomer shift IS = 0.24–0.25(1) mm s^{-1} for all samples. In the blocked state, the nuclear spin levels of the ^{57}Fe probe are split by the magnetic interactions, yielding a six-line Mössbauer spectrum. For a few-nanometre sized particle, it is known that surface contributions become increasingly important, resulting in a experimentally observed decrease of hyperfine magnetic fields B_{hyp}, assigned to weaker exchange fields sensed by the atoms at the surface [25]. For the present particles with average diameters $\langle d \rangle \approx 2.4$–$4.0$ nm (corresponding to a few multiples of the lattice parameter), about 75–80% of the spins will be located at the surface of the particle. Accordingly, the resulting spectra at $T = 4.2$ K (figure 5) were composed of an unresolved distribution of magnetic sextets reflecting the different local Fe environments and, therefore, hyperfine field distributions were used for fitting the low-temperature spectra. The resulting parameters (table 1) showed a reduced value of hyperfine fields (both the maximum B_{max} and mean B_{mean} values) for sample W10 that increase smoothly for the larger particle sizes, reflecting the large surface effects of the smallest particles. For samples W15, W20, and W30 the hyperfine parameters are in agreement with six-line ferrihydrite though with a slightly reduced B_{max} when compared to the corresponding values in 'well-crystallized' six-line ferrihydrite [24]. This B_{max} decrease could be related to lattice defects (vacancies). It is possible to observe that the second moment $\mathfrak{V}$ of the distribution, which describes how the fields are distributed around B_{mean}, steadily decreases with increasing particle size. For sample W30 the distribution is quite narrow, and the profile shows an incipient shoulder at $B \approx 44$ T. This shoulder suggests a difference between surface and core spin environments for the largest particles. For sample W20 this shoulder is still noticeable, but for smaller particles (samples W15 and W10) the spin environments of the surface and core become increasingly alike, the corresponding

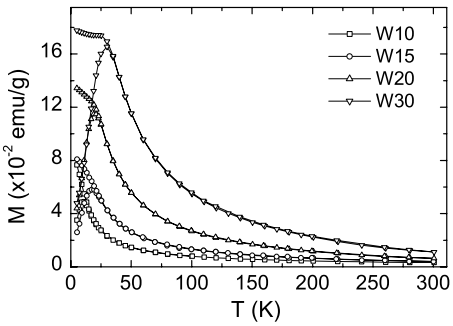

Figure 6. Temperature variation of magnetization for $H = 100$ Oe in field-cooled (FC) and zero-field-cooled (ZFC) conditions.

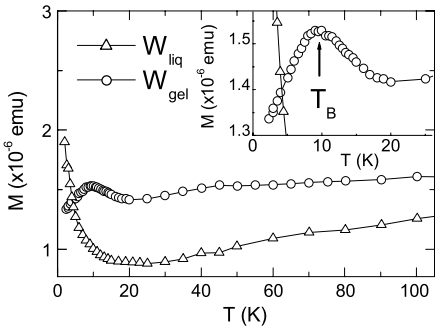

Figure 7. Magnetization curves in ZFC modes of the liquid precursor *as prepared* (W_{liq}) and lyophilized (W_{gel}). The inset shows a magnification of the ZFC peak for W_{gel}, indicating long-range magnetic order.

hyperfine fields merge with each other and the resulting distributions become broader.

3.3. Magnetization data

The magnetization curves $M(T)$ taken in field-cooling (FC) and zero-field-cooling (ZFC) modes with $H = 100$ Oe are shown in figure 6. The maxima of the ZFC branches, from which the blocking temperature T_B^m is usually defined, shifts smoothly to larger temperatures for increasing W values (table 1). It is well known that interparticle interactions can influence the blocking process and even the magnetic dynamics of the system [16]. The interparticle interactions are mainly determined by the ratio of the average distance between particles to their size. For the present concentrated (powder) samples dipolar interactions (DIs) are likely to exist and to influence to some extent the magnetic behaviour, although we are unable to quantify these parameters. However, the fact that W10 and W_{gel} samples, with identical particle size but different interparticle distances shown nearly identical blocking temperatures (figures 6 and 7 and discussion below) suggest that the DIs are not the dominating contribution to the energy barrier in these particles. For each sample, both ZFC and FC curves (measured for increasing temperatures) merge with each other at temperatures T_{rev} very close to ($\approx$2 K above) T_B^m, and the system displays full reversibility above this temperature. In real systems the distribution of particle sizes yields a distribution of T_B, so that T_{rev} can only be reached when all particles, including the largest ones, become unblocked. The close values between T_B^m and T_{rev} is a clear

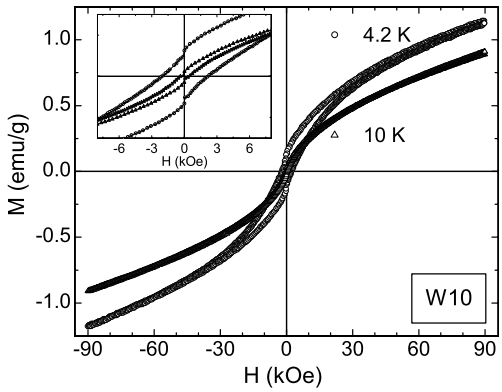

Figure 8. Magnetization of sample W10 at $T = 4.2$ and 10 K showing the large coercive field and a non-saturation up to 9 T.

indication of the extremely narrow distribution of particle sizes in our samples.

In order to see whether the magnetic phase is formed inside the reverse micelles in the liquid state, we measured the $M(T)$ curves for the precursor aqueous solutions. Figure 7 shows the results for the precursor liquid having molar ratio W = 10 (i.e., identical to the W10 sample). The observed paramagnetic behaviour down to $T = 1.8$ K demonstrates that no formation of phases with long-range magnetic order occurs at the liquid stage of the synthesis process. To further investigate the formation process, the original solution was liophylized at $P \approx 10^{-4}$ Torr during 1 h, until most of the liquid was freeze-dried. The resulting ZFC curve of W_{gel} (figure 7) shows a maximum in the ZFC branch, clearly showing the development of the magnetic phase having large-range magnetic order. The position of this maximum, located at the same temperature $T_B^m = 10.0(5)$ K as that of the corresponding W10 sample, indicates that particles with the same average particle size are present in both W_{gel} and W10 samples. The above results support the idea that the particle growth is limited by the micelles, whose boundary determines the final particle volume.

The magnetization as a function of applied fields $M(H)$ taken at $T = 4.2$ K showed non-saturating behaviour up to $H = 9$ T (see figure 8), with coercive field values $H_C \simeq 1.2$ kOe, which are compatible with previously reported values for this material [24]. This non-saturating behaviour has been explained by Néel as originated in the contribution of the core susceptibility χ_a of the antiferromagnetic (AFM) fine particles [13]. The coercivity of the particles was found to vanish very close from T_B of each sample, as observed in figure 8 for sample W10, showing almost no coercivity already at $T = 10$ K.

3.4. Susceptibility measurements

A typical set of data from the real $\chi'(f, T)$ and imaginary $\chi''(f, T)$ components of the ac susceptibility is shown in figure 9. Similar trends were observed for all samples. Both components of $\chi(f, T)$ exhibit the expected behaviour for SPM systems, i.e., the occurrence of a maximum at a temperature T_m that shifts towards higher values with increasing frequency [16]. It can be observed from table 1

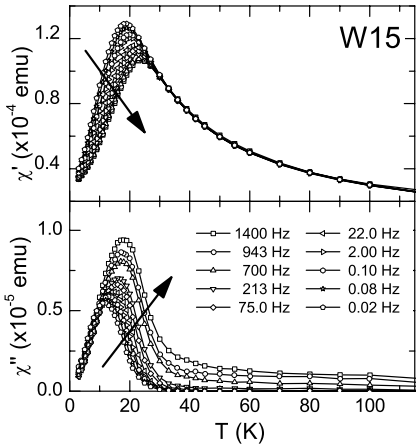

Figure 9. Typical set of the real component of ac susceptibility data $\chi'(f, T)$ as a function of temperature at different applied frequencies (upper side) and the corresponding imaginary component $\chi''(f, T)$ (bottom side).

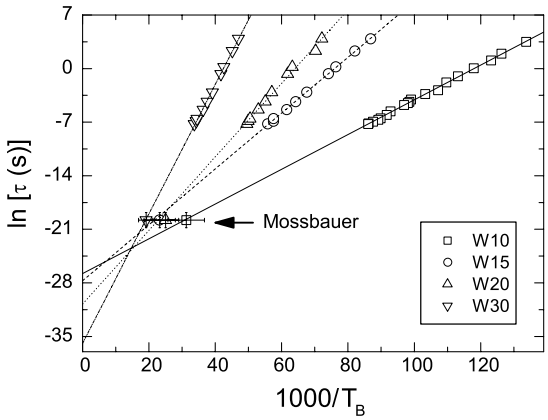

Figure 10. Blocking temperature $T_B(\ln f, H)$ dependence from $\chi''(f, T)$ data at $H = 40$ Oe. The values of T_B extracted from Mössbauer measurements are also plotted. The solid lines represent the best fit to equation (1).

that the E_a^{ac} values increase from W10 to W30 samples. The observed increase of E_a could reflect either the influence of the particle volume and/or anisotropy on the effective activation energy $E_a = K_{eff}V$, since our results clearly show (see figure 10) that the Néel–Arrhenius model correctly suits the behaviour of all samples. However, although the relaxation times τ of all samples exhibit exponential dependence on temperature (equation (1)), the fitted values of τ_0 are increasingly smaller than the $\tau_0 \approx 10^{-9}$–10^{-11} s expected for SPM systems. Both effects (i.e., increase in energy barriers and small relaxation times) are known to occur in system of interacting particles [16, 26] where, in addition to the contributions from the intrinsic particle anisotropy to E_a such as shape, magnetocrystalline, or stress anisotropies, interparticle interactions (dipolar or exchange) can also modify the energy barrier.

The fitting of the experimental $T(f, H = 0)$ data using equation (1) and the average particle radii from XRD data yielded the values of $K_{eff} = 312 \pm 10$ kJ m^{-3}, which lies within the wide range of values reported for the effective anisotropy constant of synthetic ferrihydrite $K_{eff}^{bulk} =$ 35–610 kJ m^{-3} [27–29].

4. Discussion

Single-domain magnetic particles reverse their magnetization direction due to thermal agitation, with a characteristic time τ and, therefore, the temperature of the blocking transition depends on the window time τ_M of the experimental technique used. Typical magnetization measurement assumes τ_M^m as $\approx 10^1$–10^2 s, and Mössbauer spectroscopy $\tau_M^m \approx 10^{-8}$ s. A first estimation of the activation energy $E_a = K_{eff}V$ was made using the values of T_B^m and $\tau_M^m = 10^2$ and the relation at the SPM transition [16]

$$\ln\left(\frac{\tau}{\tau_0}\right) \approx 30 = \frac{E_a}{k_B T_B}. \qquad (2)$$

The resulting E_a^{ZFC} values are included in table 1. The observed increase of E_a^{ac} could be attributed to the increasing particle volume on the energy barriers of the system. It is known that the ratio between the average distances and sizes of the particles usually determines how much the interaction influences T_B. For example, at low concentrations the interaction is weak and therefore the single-particle anisotropy is dominant. However, as already discussed for ac susceptibility data, these values are obtained in non-diluted samples and thus they include the (unknown) contribution from magnetic dipolar interactions to the effective anisotropy constant K_{eff}. Since the samples are in the concentrated regime, small changes in particle volume could affect the dipolar interactions because particle diameters are comparable to the average distance between particles. The observed variation of τ_0 in figure 10 seems too large to be explained only by volume changes, so changes in the interparticle interactions cannot be discarded. The value obtained from equation (2) amounted to $K_{eff} \approx 320$–380 kJ m^{-3}, which is in agreement with the $K_{eff} = 312 \pm 10$ kJ m^{-3} value from ac susceptibility discussed above. These values are nearly two orders of magnitude larger than the usual values for iron oxides. We propose that this large value for the magnetic anisotropy is mainly related to the ferrihydrite phase, and give some arguments below.

The fit of the frequency dependence (figure 10) gave very close values of magnetic anisotropy for all samples, suggesting that the slight spread in K_{eff} values is related to experimental sources of error. Although this value obtained for the present non-diluted system also includes the effects of dipolar interactions, such a large value suggests other sources of anisotropy. Shape anisotropy is not expected to be the main contribution due to the spherical morphology observed from TEM images. We have estimated the shape contribution expected for deviations into a (e.g. prolate) spheroid with $r = c/a$ ($a = b$ and c are the minor and major axes, respectively), to the effective anisotropy. For the above situation, the shape-anisotropy constant is given by [30]

$$K_{shape} = \pi M^2\left[1 - \frac{3}{B^2}\left(\frac{r\ln(r+B)}{B} - 1\right)\right] \qquad (3)$$

where M is the particle magnetization and $B = \sqrt{r^2 - 1}$. An upper limit for this contribution can be estimated by setting

$r \approx 2$, and noting that particles with this ratio value, that should be easily observable, were not detected in the TEM images. Even if particles having this shape were present, they would contribute to K_{shape} with $\leqslant 75$ kJ m^{-3}, which is only 25–30% of the experimental value. It should be noted that the ferrihydrite particles retain their surfactant layer after lyophilization, and therefore exchange coupling between particles is not expected. We have discarded possible anisotropy contributions from the organic coating, since the value of the effective anisotropy is expected to decrease for increasing particle size when surface effects are dominant.

It can be noted from figure 10 that the linear fits using equation (1) extrapolate to increasingly large values at $T_B^{-1} = 0$ (i.e., τ_0) for increasing $\langle d \rangle$ values, in agreement with the expected dependence of this parameter on temperature and particle volume [31]. However, a quantitative analysis of this dependence would require a general expression for $\tau_0(V, T)$, which is not yet known [16].

In conclusion, we have succeeded in controlling the resulting particle sizes of ferrihydrite particles by varying the water and surfactant molar ratio in the reverse micelle used as a nanoreactor. The resulting magnetic behaviour reflects this control of average particle size through the smooth variation of the magnetic parameters, such as blocking temperature T_B and activation energy E_a. By investigating the thermally activated nature of the blocking process through dynamical data, a rather large anisotropy constant of $K_{eff} = 320$–380 kJ m^{-3} has been obtained. The origin of this anisotropy, which is ∼50 times larger than the typical value for iron oxides, remains uncertain, as well as the question whether it is located at the core or surface of the particles. The well-known ability of ferrihydrite to transform quite easily into other iron phases, depending on the environmental conditions [23, 32] (further favoured in nanoparticles due to the large surface area), led us to search for evidence of phase evolution in our particles. After repeating both the magnetization and Mössbauer experiments several weeks later, we obtained essentially the same results as in the fresh samples.

Acknowledgments

This work was supported in part by the Brazilian agencies FAPESP, CNPq and CAPES/Procad. ELD was a recipient of CNPQ PhD fellowship. TSB was supported by National Science Foundation (NSF) grant EAR 0311869 from the Biogeosciences program. This is IRM publication No. 0604. ELJ is grateful to the VolkswagenStiftung, Germany, for providing financial support through a Postdoctoral Fellowship. GFG acknowledges financial support from the Spanish Ramon y Cajal program.

References

[1] Drits V A, Sakharov B A, Salyn A L and Manceau A 1993 *Clay Miner.* **28** 185
[2] Jansen E, Kyek A, Schäfer W and Schwertmann U 2002 *Appl. Phys.* A **74** 1004
[3] Murad E 1996 *Phys. Chem. Minerals* **23** 248
[4] Murad E and Schwertmann U 1980 *Am. Mineral.* **65** 1044
[5] Jolivet J P, Chanéac C and Tronc E 2004 *Chem. Commun.* **5** 477
[6] Punnoose A, Phanthavady T, Seehra M S, Shah N and Huffman J P 2004 *Phys. Rev.* B **69** 054425
[7] Cornell R M and Schwertmann U 1996 *The Iron Oxides: Structure, Properties, Reactions, Occurrences and Uses* (Wenheim: Wiley–VCH)
[8] Pardoe H, Chua-anusorn W, St Pierre T G and Dobson J 2003 *Phys. Med. Biol.* **48** N89
[9] Bell S H, Weir M P, Dickson D P E, Gibson J F, Sharp G A and Peters T J 1984 *Biochim. Biophys. Acta* **787** 227
[10] Bauminger E P and Nowik I 1989 *Hyperfine Interact.* **50** 489
[11] Kilcoyne S H and Cywinsky R 1995 *J. Magn. Magn. Mater.* **140** 1466
[12] Makhlouf S A, Parker F T and Berkowitz A E 1997 *Phys. Rev.* B **55** R14–717
[13] Néel L 1961 *C. R. Acad. Sci.* **253** 9
[14] Néel L 1949 *Ann. Geophys.* **5** 99
[15] Mørup S 1990 *Hyperfine Interact.* **60** 959
[16] Dormann J L, Fiorani D and Tronc E 1997 *Adv. Chem. Phys.* **98** 283
[17] Hochepied J F, Bonville P and Pileni M P 2000 *J. Phys. Chem.* B **104** 905
[18] O'Connor C J, Seip C T, Carpenter E E, Li S and John V T 1999 *Nanostruct. Mater.* **12** 65
[19] Liu C, Zou V S, Rondinone A J and Zhang Z J 2000 *J. Phys. Chem.* B **104** 1141
[20] Carpenter E E and O'Connor C J 1999 *J. Appl. Phys.* **85** 5175
[21] Motte L, Billoudet F and Pileni M P 1995 *J. Phys. Chem.* **99** 16425
[22] Klug H P and Alexander L E 1974 *X-ray Diffraction Procedures for Polycrystalline and Amorphous Materials* 2nd edn (New York: Wiley–Interscience)
[23] Jambor J L and Dutrizac J E 1998 *Chem. Rev.* **98** 2549
[24] Guyodo Y, Banerjee S K, Penn R L, Burleson D, Berquó T S, Seda T and Solheid P 2006 *Phys. Earth Planet. Int.* **157** 222
[25] Rusponi S, Cren T, Weiss N, Epple M, Buluschek P, Claude L and Brune H 2003 *Nat. Mater.* **2** 546
[26] Arelaro A D, Brandl A L, Lima E Jr and Goya G F 2005 *J. Appl. Phys.* **97** 014133
[27] Suzdalev I P, Buravtsev V N, Imshennik V K, Maksimov Yu V, Matveev V V, Novichikhin S V, Trautwein A X and Winkler H 1996 *Z. Phys.* D **37** 55
[28] Gilles C, Bonville P, Wong K K W and Mann S 2000 *Eur. Phys. J.* B **17** 417
[29] Harris J G E, Grimaldi J E, Awschalom D D, Chiolero A and Loss D 1999 *Phys. Rev.* B **60** 3453
[30] Aharoni A 1998 *J. Appl. Phys.* **83** 3432
[31] Nowak U, Mryasov O N, Wieser R, Guslienko K and Chantrell R W 2005 *Phys. Rev.* B **72** 172410
[32] Eggleton R A and Fitzpatrick R W 1988 *Clays Clay Miner.* **36** 111